

# Characteristics of Spontaneous Anterior–Posterior Oscillation-Frequency Convergences in the Alpha Band

Satoru Suzuki,<sup>1</sup> Marcia Grabowecy,<sup>1</sup> and Melisa Mencilglu<sup>2</sup>

<sup>1</sup>Department of Psychology and Interdepartmental Neuroscience, Northwestern University, Evanston, Illinois 60208 and <sup>2</sup>Cognitive, Linguistic, and Psychological Sciences, Brown University, Providence, Rhode Island 02912

## Abstract

Anterior–posterior interactions in the alpha band (8–12 Hz) have been implicated in various functions including perception, attention, and working memory. The underlying neural communication can be flexibly controlled by adjusting phase relations when activities across anterior–posterior regions oscillate at a matched frequency. We thus investigated how alpha oscillation frequencies spontaneously converged along anterior–posterior regions by tracking oscillatory EEG activity while participants rested. As more anterior–posterior regions (scalp sites) frequency-converged, the probability of additional regions joining the frequency convergence increased, and so did oscillatory synchronization (i.e., oscillatory power) at participating regions, suggesting that anterior–posterior frequency convergences are driven by inter-regional entrainment. Notably, frequency convergences were accompanied by two types of approximately linear phase gradients, one progressively phase lagged in the anterior direction, the posterior-to-anterior (P-A) gradient, and the other progressively phase lagged in the posterior direction, the anterior-to-posterior (A-P) gradient. These gradients implied traveling waves propagating in the feedforward and feedback directions, respectively. Interestingly, while in natural viewing frequency convergences were accompanied by both gradient types (occurring at different frequencies) regardless of anterior–posterior routes, when the eyes were closed, the P-A and A-P gradients spatially segregated, channeling feedforward flows of information primarily through the midline and feedback flows primarily through each hemisphere. Future research may investigate how eye closure organizes information flows in this way and how it influences hierarchical information processing. Future research may also investigate the functional roles of frequency-convergence contingent traveling waves in contrast to those generated by other mechanisms.

**Key words:** alpha band; frequency convergence; human EEG; neural oscillation

## Significance Statement

Anterior–posterior interactions in the alpha band (8–12 Hz) have been implicated in perception, attention, and working memory. While alpha frequencies differ across anterior–posterior regions, they also dynamically converge while people rest. Our EEG study investigated the mechanisms and functions of spontaneous alpha-frequency convergences. Our results suggest that anterior–posterior frequency convergences are driven by inter-regional entrainment. Notably, frequency convergences were accompanied by approximately linear posterior-to-anterior and anterior-to-posterior phase gradients, likely facilitating feedforward and feedback information flows via travelling waves. Interestingly, closing the eyes spatially organized these information flows, channeling feedforward flows through the midline and feedback flows through each hemisphere. Future research may investigate the behavioral significance of these frequency-convergence contingent flows of information.

Received Jan. 16, 2024; revised Jan. 17, 2025; accepted Feb. 19, 2025.

The authors declare no competing financial interests.

Author contributions: S.S. and M.M. designed research; S.S., M.G., and M.M. performed research; S.S. and M.M. analyzed data; S.S., M.G., and M.M. wrote the paper.

This work was supported by National Institute of Neurological Disorders and Stroke (Training Program in the Neuroscience of Human Cognition) Grant T32NS047987 to M.M.

Correspondence should be addressed to Satoru Suzuki at satoru@northwestern.edu.

Copyright © 2025 Suzuki et al. This is an open-access article distributed under the terms of the [Creative Commons Attribution 4.0 International license](https://creativecommons.org/licenses/by/4.0/), which permits unrestricted use, distribution and reproduction in any medium provided that the original work is properly attributed.

## Introduction

Oscillatory neural activity is prevalent in the brain (Buzsaki, 2006). In particular, inter-regional phase locking of oscillatory activity has been proposed to play a crucial role in controlling neural communication (Fries, 2005, 2015), spurring much research examining inter-regional phase coherence within and between frequency bands. Most studies measured phase coherence as a period of stable phase difference,  $\Delta\phi(t) = n\phi_A(t) - m\phi_B(t) \sim \text{constant}$ , between signals from a pair of brain regions *A* and *B* at frequencies of a ratio, *m:n* [where  $\phi_A(t)$  and  $\phi_B(t)$  are instantaneous phases at regions *A* and *B* obtained by Hilbert transforming band-passed signals, convolving with Morlet wavelets, etc.]. For example, one would set  $m = n = 1$  for examining within-frequency phase coherence,  $m = 1$  and  $n = 3$  for examining cross-frequency phase coherence between *f* and  $3 \times f$ , and so on. Those studies primarily focused on identifying frequency-specific functional networks organized by within- and/or cross-frequency phase coherence in specific frequency bands. Extensive research using this approach has identified a variety of frequency-specific functional networks and elucidated how they contribute to perceptual, attentional, and cognitive processes (Palva et al., 2005; Palva and Palva, 2012; Lobier et al., 2018; Marzetti et al., 2019).

Focusing on phase coherence in band-passed signals, however, obscures the fact that oscillation frequencies generally differ across brain regions (Keitel and Gross, 2016; Mahjoory et al., 2020) as well as fluctuate over time (Mierau et al., 2017; Benwell et al., 2019). In order for a pair of regions to stably interact through oscillatory phase locking, their oscillation frequencies need to converge (to the same frequency for within-frequency oscillatory interactions, which is the focus of the current study, or to frequencies of a ratio, *m:n*, for cross-frequency oscillatory interactions). Thus, a complementary approach to examining inter-regional oscillatory interactions is to track oscillation frequencies in multiple regions over time and examine how they dynamically converge. Oscillation frequency in each region (e.g., an intracranial electrode, EEG/MEG scalp site, inferred source, etc.) can be tracked by applying time–frequency decomposition (e.g., using Morlet wavelets) with appropriate spectral and temporal resolution, then tracking spectral-power ridges (or stationary-phase points where  $\frac{d\text{Phase}}{dt} = 2\pi f$ ) as a function of time (Amor et al., 2005; Rudrauf et al., 2006; Mallat, 2009). Using this method, previous studies have examined spontaneous inter-regional oscillation–frequency convergences in pre-seizure neural activity (Amor et al., 2005; Rudrauf et al., 2006) as well as frequency convergences to perceived visual flicker during binocular rivalry using frequency-tagged stimuli (Rudrauf et al., 2006).

Our goal here was to uncover macroscopic rules governing spontaneous inter-regional oscillation–frequency convergences during rest using scalp-recorded EEG. What mechanisms drive oscillation frequencies in different regions to converge? What functions might inter-regional oscillation–frequency convergences serve? We sought clues to answering these questions by examining the spreading of oscillation–frequency convergences in relation to oscillatory power and phase relations.

We focused on oscillation–frequency convergences along the anterior–posterior axis partly because neural communication between anterior and posterior brain regions has been implicated in a variety of perceptual, attentional, and cognitive processes (de Pasquale et al., 2012; Gonzalez-Castillo and Bandettini, 2018; Lobier et al., 2018; Marzetti et al., 2019; Reinhart and Nguyen, 2019; Mashour et al., 2020) and partly because consistent anterior–posterior gradients of neuroanatomical and neurophysiological features have been reported, including neuron density, myelination, cortical thickness, functional-connectivity patterns, temporal integration, and oscillation frequency (Burt et al., 2018; Huntenburg et al., 2018; Mahjoory et al., 2020; Smith et al., 2024). We tracked oscillation frequencies in the alpha band because alpha oscillations have been implicated in a variety of perceptual, attentional, and memory processes (Palva and Palva, 2007; Busch and VanRullen, 2010; Mathewson et al., 2010; Klimesch, 2012; Bonnefond and Jensen, 2015; Fries, 2015; Harris et al., 2018; Lobier et al., 2018; Reinhart and Nguyen, 2019), have been shown to influence gamma band activity (Bahramisharif et al., 2013; Esghaei et al., 2022), and may organize information flow (Jensen et al., 2014; Muller et al., 2018; Zhang et al., 2018).

We examined the dynamics of spontaneous anterior–posterior oscillation–frequency convergences in an extended alpha range (5–15 Hz, accommodating the broad range, 6–13 Hz, of individual differences in primary alpha oscillation frequency; Chapeton et al., 2019) in representative rest conditions, while participants rested with their eyes closed, rested with their eyes open in a dark room, or viewed a silent nature video. We examined the spreading, power, and phase characteristics of inter-regional oscillation–frequency convergences to infer their potential mechanisms and functions. Overall, our results suggest that inter-regional entrainment drives anterior–posterior oscillation–frequency convergences in the alpha band, which may coordinate feedforward and feedback flows of information via traveling waves.

## Materials and Methods

### Participants

Fifty-two Northwestern University students (35 women, one nonbinary; mean age of 20.8 years, ranging from 18 to 29 years, standard deviation of 2.5 years) gave informed written consent to participate for monetary compensation (\$10 per hour). All participants were right-handed, had normal hearing and normal or corrected-to-normal vision, and had no history of concussion. They were tested individually in a dimly lit or darkened room in the period between 5/11/2017 and 1/27/2020. The study protocol was approved by the Northwestern University Institutional Review Board. A group of 24 individuals participated in a rest-with-eyes-closed condition in which EEG was recorded for

~5 min while participants rested with their eyes closed and *ad libitum* engaged in spontaneous thoughts. A second (nonoverlapping) group of 24 individuals participated in a replication of the rest-with-eyes-closed condition and subsequently participated in a rest-with-eyes-open-in-the-dark condition which was the same as the former except that the room was darkened and participants kept their eyes open while blinking naturally. A third group of 21 individuals (17 of whom previously participated in the rest-with-eyes-closed condition) participated in a view-silent-nature-video condition in which EEG was recorded for ~5 min while they viewed a silent nature video. To evaluate test-retest reliability, the view-silent-nature-video condition was run twice (20–30 min apart), referred to as earlier viewing and later viewing. A generic nature video was presented on a 13 inch 2017 MacBook Pro equipped with a 2880 (horizontal)-by-1800 (vertical)-pixel-resolution LCD display with normal brightness and contrast settings, placed 100 cm in front of participants, subtending ~16° (horizontal)-by-10° (vertical) of visual angle. Subsets of these data were previously analyzed for different purposes (Mencelglu et al., 2020a,b, 2021a,b, 2024).

### EEG recording and preprocessing

EEG was recorded from 64 scalp electrodes (although we used a 64-electrode montage, we excluded signals from noise-prone electrodes, Fpz, Iz, T9, and T10, from analyses) at a sampling rate of 512 Hz using a BioSemi ActiveTwo system (see [www.biosemi.com](http://www.biosemi.com) for details), while participants rested with their eyes closed, rested with their eyes open in the dark, or viewed a silent nature video for ~5 min. Electrooculographic activity was monitored using four face electrodes, one placed lateral to each eye and one placed beneath each eye. Two additional electrodes were placed on the left and right mastoids. The EEG data were preprocessed using EEGLAB and ERPLAB toolboxes for MATLAB (Delorme and Makeig, 2004; Lopez-Calderon and Luck, 2014). The data were rereferenced off-line to the average of the two mastoid electrodes and high-pass filtered at 0.01 Hz to remove drift.

### Estimating dura sources by surface-Laplacian transforming EEG signals

EEG source reconstruction methods constrained by structural MRI and fMRI localizers obtained from each participant can achieve superior source reconstruction with a brain model customized for each participant (Cottreau et al., 2015). Such an approach, however, was unavailable to us as we had neither structural MRI nor fMRI data for our participants. Among the noncustomized source-imaging methods, we chose the surface-Laplacian transform that (theoretically) estimates the spatial distribution of macroscopic current sources and sinks on the dura surface. The surface-Laplacian transform has been shown to produce similar sources to those inferred by deconvolving scalp EEG potentials using a generic model of thicknesses and impedances of the scalp and skull (Nunez et al., 1994). The surface-Laplacian transform has also been shown to approximate simulated sources and/or to extract neural correlates of some behavioral performances to a similar degree to commonly used source-imaging methods such as sLORETA and Beamforming (Tenke and Kayser, 2012; Cohen, 2015). Furthermore, there is no evidence (to our knowledge) to suggest that the latter source-imaging methods provide greater spatial resolution than the surface-Laplacian transform. Thus, our preference was to use the surface-Laplacian transform which is the most general source-imaging method that relies the least on model-specific assumptions and free parameters (Hjorth, 1980; Nunez et al., 1994; Kayser and Tenke, 2006; Nunez and Srinivasan, 2006; Tenke and Kayser, 2012).

The surface-Laplacian transform is expected to reduce volume conduction effects from substantially larger than 5 cm in raw EEG to within 1–3 cm (Nunez et al., 1994; Tenke and Kayser, 2012; Cohen, 2014; Mencelglu et al., 2024) which approximately corresponded to the average spacing of electrodes in our 64-channel montage. For our implementation of the surface-Laplacian transform, we used Perrin and colleagues' algorithm (Perrin et al., 1987, 1989, 1990) with a "smoothness" value,  $\lambda = 10^{-5}$  (recommended for 64 channels; Cohen, 2014). We surface-Laplacian transformed all EEG signals and refer to those signals that represent the macroscopic current sources and sinks on the dura surface under the 60 scalp sites (with the four noise-prone sites excluded from the analyses) simply as EEG signals.

### EEG analysis

*Taking the temporal derivative.* We needed to track spectral ridges (likely indicative of oscillation frequencies) at sub-second temporal resolution. The aperiodic  $1/f^\beta$  spectral background in EEG may interfere with the identification of spectral ridges. A commonly employed strategy to circumvent this problem is to compute FFTs over partially overlapping time windows of several seconds or longer and then fit a power function to each time-windowed FFT to remove the  $1/f^\beta$  component (Chiang et al., 2011; van Albada and Robinson, 2013; Donoghue et al., 2020). However, it is difficult to reliably estimate the  $1/f^\beta$  component on a subsecond timescale. Note that  $\beta$  in the  $1/f^\beta$  spectral background varies around the value of 1 (see He, 2014, for a review of the various factors that influence  $\beta$ , and Gao et al., 2017, for contributions of excitatory and inhibitory dynamics to  $\beta$ ). Although taking the temporal derivative of EEG ( $\frac{\Delta \text{EEG}}{\Delta t}$ , where  $\Delta t$  is the temporal resolution, i.e., 1/512 s) would completely neutralize the  $1/f^\beta$  component only when  $\beta = 1$ , the method worked well in our prior studies (Mencelglu et al., 2021a,b, 2024, Smith et al., 2024). Specifically, any time series,  $f(t)$ , can be expressed as an integral over its sinusoidal components,  $f(t) = \frac{1}{\sqrt{2\pi}} \int_{-\infty}^{\infty} g(\omega) e^{i\omega t} d\omega$  with  $g(\omega) = \frac{1}{\sqrt{2\pi}} \int_{-\infty}^{\infty} f(t) e^{-i\omega t} dt$ , where  $\omega/2\pi$  is frequency (Fourier's theorem). Because taking the temporal derivative merely multiplies each sinusoidal component by its frequency (from the chain rule of differentiation), taking the temporal derivative adds a log-log slope of 1 to an amplitude spectrum to cancel the log-log slope of the aperiodic component, which is  $-1$  if  $\beta = 1$ . If  $\beta$  is different than 1, taking the temporal derivative will either under- or overcompensate for the negative aperiodic slope. For the EEG data analyzed here, taking the

temporal derivative effectively reduced or removed the negative slopes of the aperiodic components (not shown, but equivalent to the comparison plots shown for similar data in Fig. 1 in Smith et al., 2024).

**Time–frequency decomposition using Morlet wavelets.** To track EEG power spectra at high temporal and spectral resolutions, we used a Morlet wavelet-convolution method suitable for time–frequency decomposition of signals containing multiple oscillatory sources of different frequencies (see Cohen, 2014 for a review of different methods for time–frequency decomposition). Each Morlet wavelet is a Gaussian-windowed complex sinusoidal template characterized by its frequency as well as its temporal and spectral widths that limit its temporal and spectral resolution. We convolved each EEG waveform (i.e., its temporal derivative) with a set of wavelets tuned to a range of frequencies, yielding a time series of complex values per wavelet frequency. The power and phase of each extracted sinusoidal component at each timepoint were given by the modulus squared (power) and the arc tangent of the ratio of the imaginary component to the real component (phase). We used a set of wavelets with 160 frequencies,  $f'_w$ s, ranging from 5 to 15 Hz (accommodating individual differences, 6–13 Hz, in primary alpha oscillation frequency; Chapeton et al., 2019). The  $f'_w$ s were logarithmically spaced as neural temporal-frequency tunings tend to be approximately logarithmically scaled (Hess and Snowden, 1992; Lui et al., 2007). The accompanying  $m$  parameter (roughly the number of cycles per wavelet, with the precise definition,  $m = 2\pi f \cdot \text{SD}$ , where SD is the wavelet standard deviation) was also logarithmically spaced between 11.7 and 35, yielding a temporal resolution of  $\text{SD} = 370$  ms and a spectral resolution of FWHM (full-width at half-maximum of wavelet spectrum) = 1.0 Hz that were virtually invariant across the wavelet frequencies.

**Identifying oscillation frequencies per timepoint.** Oscillation frequencies are typically identified as spectral peaks (a.k.a. ridges) that theoretically coincide with points of phase stationarity (Mallat, 2009). However, when multiple oscillations at neighboring frequencies coincide, each oscillation frequency does not necessarily generate a local maximum in the power spectrum due to limited spectral resolution. An example is shown in Figure 1A, plotting a power spectrum at a single timepoint obtained with our Morlet wavelets for simulated data containing five sinusoidal oscillations at 6, 7, 9.5, 10.5, and 13 Hz (vertical arrows) of different amplitudes. Only three of the five oscillation frequencies were identified as spectral peaks (Fig. 1A, black open circles) which coincided with points of phase stationarity (the negatively sloped zero crossings of  $\frac{d\text{Phase}}{dt} - 2\pi f$  shown in Fig. 1B). Overshadowed by the neighboring high-amplitude oscillations at 6 and 10.5 Hz, the low-amplitude oscillations at 7 and 9.5 Hz did not generate peaks (Fig. 1A). However, it is evident that the low-amplitude oscillations generated “shoulders” within the larger profiles generated by the neighboring high-amplitude oscillations. Note that these spectral shoulders as well as spectral peaks generate curvature maxima. We thus identified oscillations as curvature maxima. As shown in Figure 1A, the low-amplitude oscillations at 7 and 9.5 Hz were successfully detected as curvature maxima (red open circles) though they generated neither spectral peaks nor points of phase stationarity.

The location of each spectral peak was identified as the frequency at which the power value was higher than those at the neighboring sampled frequencies. The spectral curvature at each frequency was computed discretely as the second

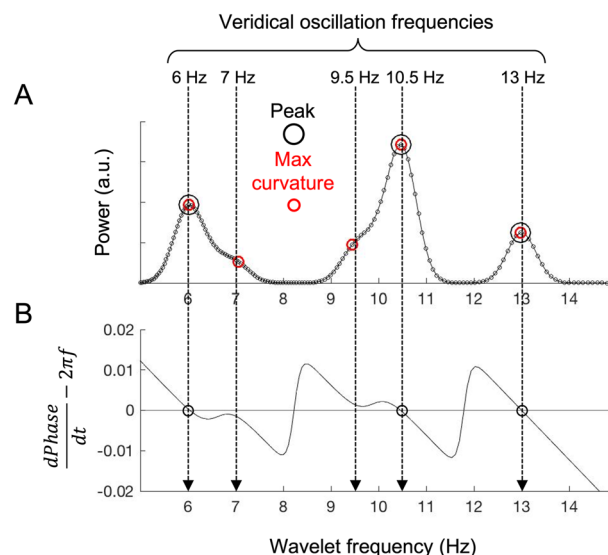


**Figure 1.** Identifying oscillation frequencies as curvature maxima in a power spectrum. **A**, A power spectrum (for a single timepoint) of simulated EEG data containing sinusoidal oscillations at 6, 7, 9.5, 10.5, and 13 Hz (vertical arrows) of various amplitudes obtained with our 160 wavelets tuned to log-spaced frequencies between 5 and 15 Hz. The large black circles indicate oscillation frequencies identified as spectral peaks, whereas the red circles indicate oscillation frequencies identified as curvature maxima. Note that only curvature maxima identified the low-amplitude oscillations at 7 and 9.5 Hz occurring near the high-amplitude oscillations at 6 and 10.5 Hz. **B**, A plot of  $\frac{d\text{Phase}}{dt} - 2\pi f$  as a function of  $f$  (wavelet frequency). The negatively sloped zero crossings (black circles) indicate the points of phase stationarity, which coincide with the spectral peaks in **A**.

derivative of spectral power (with respect to frequency),  $Pow''_{f_i} = (Pow_{f_{i+1}} - Pow_{f_i}) - (Pow_{f_i} - Pow_{f_{i-1}})$ , where  $Pow''_{f_i}$  is the second derivative at frequency  $f_i$ ,  $Pow_{f_i}$  is the power value at  $f_i$ , and  $Pow_{f_{i+1}}$  and  $Pow_{f_{i-1}}$  are the power values at the neighboring sampled frequencies. The location of each curvature maximum was identified as the frequency at which  $Pow''$  was negative and more negative than those at the neighboring sampled frequencies (given that negative local minima of the second derivative correspond to spectral bumps).

We tracked curvature maxima as a function of time at anterior–posterior sites along the midline (AFz, Fz, FCz, Cz, CPz, Pz, POz, and Oz), left-hemisphere (AF3, F3, FC3, C3, CP3, P3, PO3, and O1), and right-hemisphere (AF4, F4, FC4, C4, CP4, P4, PO4, and O2) routes. It is likely that some of the curvature maxima associated with low powers were due to noise. Nevertheless, instead of imposing an arbitrary power threshold, we analyzed data relative to their time-shuffled controls as described below. The effects of spurious curvature maxima due to noise were discounted by comparing actual data with their time-shuffled controls.

*Computing a frequency-convergence matrix containing frequency convergence sizes (one through eight sites) across frequencies (rows) and timepoints (columns).* We considered oscillation frequencies from a pair of sites to be converged when they were within  $\pm 1.4\%$ . This was equivalent to having an overlap when each oscillation frequency was broadened by  $\pm 1$  log unit (recall that we logarithmically sampled wavelet frequencies). This  $\pm 1.4\%$  criterion balanced precision in detecting frequency convergences with the need for detecting sufficient instances of frequency convergences for meaningful statistical analysis.

For each site (for each participant and behavioral condition), we organized the time-varying oscillation frequencies in an oscillation-frequency-(row)-by-time-(column) matrix. An *oscillation-frequency matrix* was initially filled with zeros. Then, we filled the matrix element corresponding to each identified oscillation frequency at each timepoint as well as the rows immediately above and below it with ones (broadening each oscillation frequency by  $\pm 1$  log unit; see above). Thus, each oscillation frequency at each timepoint was indicated by a vertical triplet of ones. To obtain a *frequency-convergence matrix* filled with oscillation-frequency convergence sizes (one through eight sites), we stacked the oscillation-frequency matrices from eight anterior–posterior sites on top of one another and summed them across the vertical dimension, yielding an oscillation-frequency-(row)-by-time-(column) matrix filled with values 1 through 8 corresponding to frequency-convergence sizes.

How oscillation frequencies dynamically converged across anterior–posterior sites can be visualized by plotting a frequency-convergence matrix. An example is shown in Figure 2 for one participant in the rest-with-eyes-closed condition; the cooler/darker colors indicate frequency convergences (along the midline) across larger numbers of anterior–posterior sites.

*Using time-shuffled frequency-convergence matrices as a control.* Some of the observed oscillation-frequency convergences may be due to coincidences (across anterior–posterior sites) of alpha oscillations at dominant frequencies ( $\sim 10$  Hz) and/or coincidences of low-power oscillations attributable to noise. To discount these spurious contributions, we generated time-shuffled frequency-convergence matrices. Specifically, we randomly time-shifted (in a circular manner) the oscillation-frequency matrix from each site (300 s long) by between 0 and 150 s (sampled from a uniform distribution). We then vertically summed the randomly time-shifted oscillation-frequency matrices across sites to generate a time-shuffled frequency-convergence matrix. To evaluate various characteristics of oscillation-frequency convergence, we computed the relevant measures with 20 time-shuffled frequency-convergence matrices and averaged them to generate their control values.

## Results

Our goal was to uncover general characteristics of spontaneous anterior–posterior oscillation-frequency convergences to infer their mechanisms and functions. To reveal any topographic characteristics, we examined anterior–posterior oscillation-frequency convergences along the midline route and the route through each hemisphere.

### Oscillation-frequency convergences are not mere coincidences

We first confirmed that anterior–posterior oscillation-frequency convergences occurred over and above what would be expected by random coincidences. We did so by comparing the total instances of frequency convergence of each size

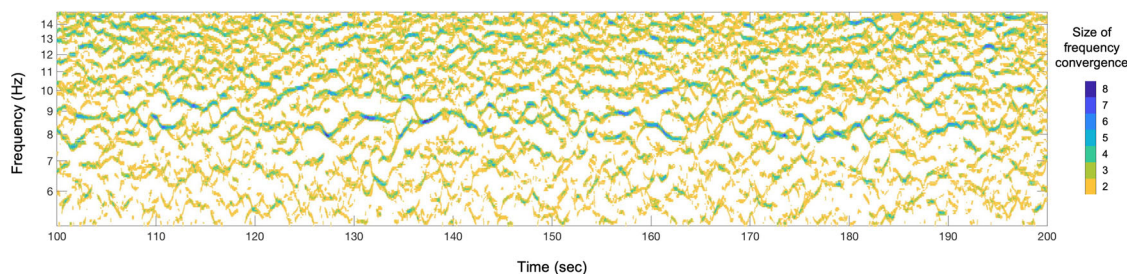


**Figure 2.** Visualization of a frequency-convergence matrix, showing the number of frequency-converged anterior–posterior sites (color coded) along the midline as a function of oscillation frequency (y-axis) and time (x-axis), for one participant in the rest-with-eyes-closed condition during a 100 s period. Cooler/darker colors indicate oscillation-frequency convergences across larger numbers of anterior–posterior sites.

(one through eight) between the actual and time-shuffled frequency-convergence matrices. The instances of frequency convergence of four or more sites were consistently elevated in the actual data (red curves) relative to the time-shuffled controls (black curves) for all participants (Fig. 3A presenting the rest-with-eyes-closed condition as a representative example; see Extended Data Fig. 3-1 for the results from all behavioral conditions). Given that the total number of instances are plotted in a log scale, the elevations were substantial (by about an order of magnitude for convergence sizes of seven and eight). Thus, anterior–posterior oscillation-frequency convergences are coordinated rather than coincidental.

To gain insights into the underlying mechanisms and functions of anterior–posterior oscillation-frequency convergences, we examined some of their general characteristics. While a variety of their spatial, spectral, and temporal features can be examined, we focused on the following questions. First, how does an oscillation-frequency convergence grow? For instance, does the probability of incorporating another site into a frequency convergence increase or decrease with the size of frequency convergence? Second, how are oscillation-frequency convergences related to oscillatory power? Third, are oscillation-frequency convergences accompanied by consistent phase relations? As discussed below, investigating these questions provided some insights into the potential mechanisms and functions of dynamic anterior–posterior oscillation-frequency convergences.

### **The probability of incorporating another site into an oscillation-frequency convergence increased as the size of frequency convergence increased**

What mechanisms drive anterior–posterior oscillation-frequency convergence? One possibility was that multiple regions could be driven to oscillate at a matched frequency via inter-regional entrainment. Spreading inter-regional entrainment would reciprocally enhance within-region synchronization (Tewarie et al., 2019), which in turn would facilitate further inter-regional spreading of entrainment. This possibility would predict that (1) a frequency convergence across more regions (sites) would be associated with higher oscillatory power (a measure of within-region synchronization) at participating sites and (2) the probability of another site joining a frequency convergence would increase as more sites frequency-converge. We evaluated Prediction 2 here and Prediction 1 in the next section.

We computed the probability of growing in frequency convergence as a function of the number of frequency-converged sites. We first obtained the average base probability of oscillatory activity by computing the proportion of ones in the oscillation-frequency matrix from each site (containing ones where oscillations were identified, broadened by  $\pm 1$  log unit; see Materials and Methods) and averaging the values across sites. We call this  $P(1)$ , the average probability of oscillatory activity. If oscillation-frequency convergences were due to random coincidences, the average probability of frequency convergence across  $k$  sites,  $P(k)$ , should be given by  $P(1)^k$ .

We computed the probability of frequency convergences across  $k > 1$  sites as follows. For each combination of  $k$  sites, we stacked and summed their oscillation-frequency matrices and computed the proportion of  $k$ 's in the resultant matrix to obtain the probability of  $k$  convergence. We then averaged the probabilities computed for all combinations of  $k$  sites to obtain the average probability of  $k$  convergence,  $P(k)$ . To estimate the probability of growing in frequency convergence at each level of convergence, we computed the conditional probability of obtaining  $k$  convergence given  $k-1$  convergence,  $P(k|k-1)$ , by dividing  $P(k)$  by  $P(k-1)$  because  $k$  convergence was a subset of  $k-1$  convergence. We computed  $P(k|k-1)$  (where  $2 \leq k \leq 8$ ) for each participant for each behavioral condition.

The probability of growing in convergence,  $P(k|k-1)$ , monotonically increased as a function of the number of frequency-converged sites,  $k$  (red curves; Fig. 3B presenting the rest-with-eyes-closed condition as a representative example; see Extended Data Fig. 3-2A for the results from all behavioral conditions). Slight increases were also observed in the time-shuffled controls (black curves), indicating that some general features of the oscillation-frequency matrices (e.g., major oscillations occurring in relatively narrow frequency ranges) slightly increased the probability of coincidental frequency convergences relative to the chance level (gray line). The data for large frequency convergences (for  $k = 7$  and especially for  $k = 8$ ) were somewhat noisy as their instances were relatively rare especially for the time-shuffled controls (Fig. 3A; Extended Data Fig. 3-1). Importantly,  $P(k|k-1)$  for the actual data increased substantially more steeply than that for the time-shuffled controls as a function of  $k$  (Fig. 3C presenting the rest-with-eyes-closed condition as a representative example; see Extended Data Fig. 3-2B for the results from all behavioral conditions). This indicates that the probability of growing in frequency convergence monotonically increased as a function of the size of frequency convergence, controlling for any potential effects of time-independent spectral features at the individual sites.

### **Larger oscillation-frequency convergences were associated with higher oscillatory power at participating sites**

Here we evaluated the other prediction that if oscillation-frequency convergences were driven by inter-regional entrainment, frequency convergences across more regions (sites) would be associated with higher oscillatory power (a measure of within-region synchronization) at participating sites.

To evaluate this possibility, we temporally averaged the powers of all oscillations at each site, separately for each size of frequency convergence,  $k$ , in which it participated. For instance, we temporally averaged the powers of oscillations at AFz when their oscillation frequencies did not converge with any other sites ( $k = 1$ ), when their oscillation frequencies converged with one other site ( $k = 2$ ), their oscillation frequencies converged with two other sites ( $k = 3$ ), and so on. This yielded the average oscillatory power at each site as a function of the size of frequency convergence in which the site participated. However, we may obtain a spurious association between higher-power and larger-frequency convergence due

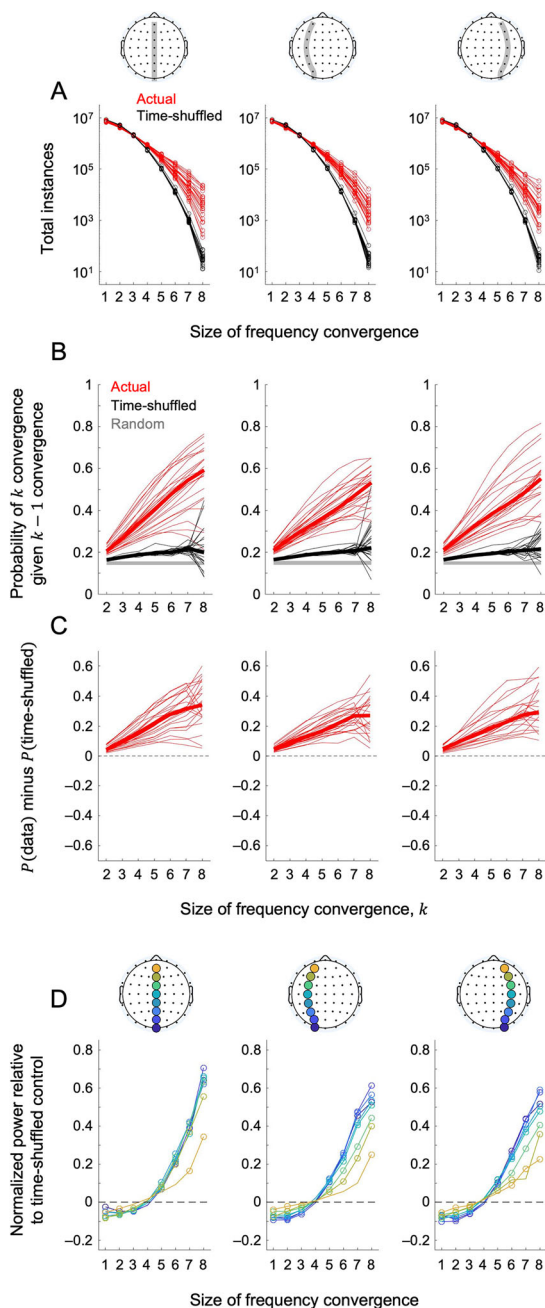


**Figure 3.** Instance, probability, and oscillatory power associated with oscillation-frequency convergence. Data for the rest-with-eyes-closed condition are presented as a representative example. **A**, Total instances of anterior–posterior oscillation–frequency convergence as a function of the size of frequency convergence, for the midline (left), left-hemisphere (middle), and right-hemisphere (right) routes. The actual data are shown in red, and the time-shuffled controls are shown in black. Each curve represents a participant. Note that the instances of frequency convergence of four or more sites were elevated in the actual data (red) relative to the time-shuffled controls (black) for all participants. Data for all behavioral conditions are presented in Extended Data Figure 3-1. **B**, The probability of  $k$  convergence (oscillation–frequency convergence across  $k$  sites) given  $k - 1$  convergence, that is, the probability of growing in convergence from  $k - 1$  to  $k$ ,  $P(k|k - 1)$ , as a function of  $k$ , for the midline (left), left-hemisphere (middle), and right-hemisphere (right) routes.  $P(k|k - 1)$  for the actual data (red) are shown with the corresponding time-shuffled controls (black) as well as  $P(k|k - 1)$  expected if oscillation–frequency convergences occurred randomly (gray). **C**,  $P(k|k - 1)$  for the actual data minus that for the corresponding time-shuffled controls. The thin lines represent data from individual participants with the thick line representing the median. Note that the probability of incorporating another site into a frequency convergence increased as more sites frequency-converged. For **(B)** and **(C)**, data for all behavioral conditions are presented in Extended Data Figure 3-2. **D**, Time-averaged oscillatory power as a function of the size of frequency convergence at each site along the anterior–posterior axis [color-coded from dark blue (posterior) to yellow (anterior)], for the midline (left), left-hemisphere (middle), and right-hemisphere (right) routes. The power values are relative to those obtained with the corresponding time-shuffled controls, normalized to the maximum actual power for each power-by-convergence curve (per site per participant). The values averaged across participants are plotted, with each open circle indicating Bonferroni-corrected statistical significance ( $\alpha = 0.05$ , two-tailed) relative to zero (control levels). Note that most sites showed accelerated increases in power when they participated in frequency convergences of four or more sites. Data for all behavioral conditions are presented in Extended Data Figure 3-3.

to time-independent spectral features. For example, if higher-power oscillations concentrated within a narrow frequency range while lower-power oscillations broadly distributed across frequencies, higher-power oscillations would coincidentally frequency-converge with a higher probability than lower-power oscillations. We thus applied the same analysis to the corresponding time-shuffled controls (see Materials and Methods).

For each site, we computed its average oscillatory power minus the value obtained from the corresponding time-shuffled control as a function of the size of frequency convergence in which the site participated. To facilitate comparisons of these power-by-convergence curves across sites, participants, and behavioral conditions, we normalized each curve (actual minus control) by dividing it by its maximum actual power (per site per participant per behavioral condition).

Figure 3D shows the (normalized) average oscillatory power at each site [color coded from dark blue (posterior) to yellow (anterior)] as a function of the size of frequency convergence in which the site participated (the rest-with-eyes-closed condition presented as a representative example; see Extended Data Fig. 3-3 for the results from all behavioral conditions). The open circles indicate Bonferroni-corrected (for eight convergence sizes) significant difference from the control level (i.e., zero) at  $\alpha = 0.05$  (two-tailed). The oscillatory power generally increased as a function of the size of frequency convergence at all sites, rising significantly above the control levels at frequency convergences of four or five sites and steeply increasing at larger convergences (except that the power did not rise significantly above the control level at the anterior-most site during the natural viewing conditions; see Extended Data Fig. 3-3, yellow curves).

These results and those presented in the preceding section are consistent with the idea that anterior–posterior oscillation–frequency convergences are driven by inter-regional entrainment that reciprocally enhances within-region synchronization (this section), which in turn facilitates further inter-regional spreading of entrainment (preceding section).

### **Anterior–posterior oscillation–frequency convergences were accompanied by approximately linear phase gradients**

What functions might anterior–posterior oscillation–frequency convergences serve? When neural activities oscillate at a matched frequency across regions, communication between them can be controlled by adjusting phase lags. We thus examined how oscillation–frequency convergences influenced phase relations. For example, if frequency convergences were accompanied by linear phase gradients, one could infer that frequency convergences facilitate directional flows of information.

We computed sequential pairwise phase differences from posterior to anterior sites. Note that choosing this direction was arbitrary; the interpretation of the results would be the same regardless of the direction in which we computed phase differences. For example, for the midline route, we computed the phase of POz minus the phase of Oz, the phase of Pz minus the phase of POz, the phase of CPz minus the phase of Pz, the phase of Cz minus the phase of CPz, the phase of FCz minus the phase of Cz, the phase of Fz minus the phase of FCz, and the phase of AFz minus the phase of Fz. These sequential phase differences were computed at each oscillation frequency at each timepoint for each pair of sites that participated in a frequency convergence between two or more sites. Then, for each pair, their phase differences were averaged (as complex angles) across all instances, separately for each size of frequency convergence. Because of this temporal averaging, this analysis detected phase relations that were consistent over the ~5 min period. The resultant time-averaged phase differences were averaged within each of the 19 partially overlapping frequency bins (1 Hz wide with 0.5 spacing).

To detect phase gradients (if any) in each frequency bin, we spatially integrated the corresponding sequential pairwise phase differences from the posterior to anterior sites (i.e., we cumulatively summed the sequential pairwise phase differences from the posterior to anterior sites) while arbitrarily setting the phase at the posterior-most site to zero. Overall, we observed two types of phase gradients (see below for details). One was negatively sloped (Fig. 4D, left) indicating that more anterior sites were more phase lagged, suggestive of a posterior-to-anterior flow of information, which we call the “posterior–anterior (P-A) gradient.” The other was positively sloped (Fig. 4D, right) indicating that more posterior sites were more phase lagged, suggestive of an anterior-to-posterior flow of information, which we call the “anterior–posterior (A-P) gradient.” It is clear from Figure 4D that both the P-A and A-P gradients developed, from barely sloped to substantially sloped, as the size of frequency convergence increased.

To verify that these phase gradients accompanying oscillation–frequency convergences were distinctive types, we examined the distribution of the negative and positive phase gradients across the frequency bins. For each frequency bin, we computed the linear trend of the overall phase gradient (averaged across frequency-convergence sizes) by computing Pearson’s  $r$  between the serial site index (1 through 8 from posterior to anterior) and the corresponding phase value. We weighted each  $r$  value by a measure of the temporal stability of the corresponding phase gradient, that is, by its average phase-locking value (PLV; Cohen, 2014; averaged across all sequential pairwise values within the gradient). We note that steeper phase gradients tended to have higher PLVs (especially in the minimal-visual-stimulation condition; Extended Data Fig. 4-1) indicating that steeper phase gradients tended to be temporally more stable. PLV’s were corrected for sample-size-dependent biases by subtracting the expected chance levels (computed with the assumption of random sampling from a uniform angular distribution, well approximated by a power function of the sample size). As the corrected PLV’s varied between close to 1, indicative of perfect phase locking, and near 0, indicative of no phase locking, the PLV-weighted  $r$  values varied between close to  $-1$ , indicative of a perfectly negative linear P-A gradient, to close to 1, indicative of a perfectly positive linear A-P gradient. For brevity, we will refer to the PLV-weighted  $r$  simply as  $r$ .



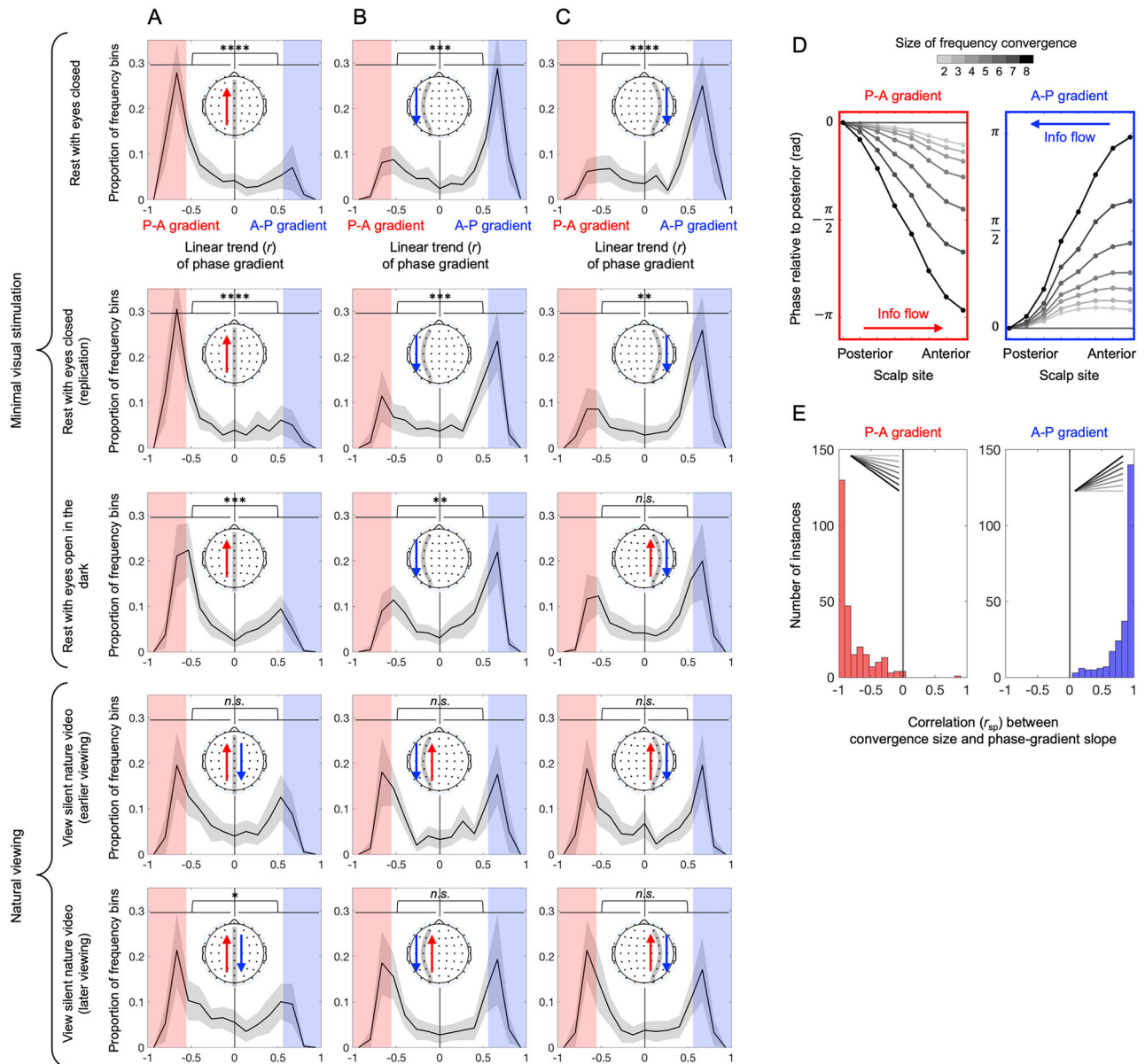


**Figure 4.** Characteristics of the anterior–posterior phase gradients accompanying oscillation–frequency convergence. **A–C**, Distribution of the linear trend (Pearson’s  $r$  weighted by PLV) of the anterior–posterior phase gradient (averaged across frequency-convergence sizes) obtained across the 19 frequency bins (1 Hz wide with 0.5 Hz spacing, spanning 5–15 Hz), for the midline (**A**), left-hemisphere (**B**), and right-hemisphere (**C**) routes. Negative values indicate the P-A gradients (with more anterior sites more phase lagged; illustrated with a single red arrow when they were prevalent), whereas positive values indicate the A-P gradients (with more posterior sites more phase lagged; illustrated with a single blue arrow when they were prevalent). The line represents the distribution averaged across participants, and the shaded area represents the 95% confidence interval. The rows represent the five behavioral conditions. Note that the distributions are bimodal for all anterior–posterior routes in all behavioral conditions, indicating that the P-A and A-P gradients are distinct types. The asterisks ( $*p < 0.05$ ;  $**p < 0.01$ ;  $***p < 0.001$ ;  $****p < 0.0001$ ) indicate  $t$  test results (two-tailed) comparing the number of negative with positive  $r$  values, testing the asymmetry of each distribution. Note that the distributions for the minimal-visual-stimulation conditions are mostly asymmetric (top three rows), whereas those for the natural viewing conditions are mostly symmetric (bottom two rows). **D**, The P-A gradient (left; identified as the gradients with  $r$  less than  $-0.6$ ; see the red-shaded regions in **A–C**) and the A-P gradient (right; identified as the gradients with  $r$  greater than  $0.6$ ; see the blue-shaded regions in **A–C**) averaged across the three anterior–posterior routes, participants, and behavioral conditions. Note that both gradients developed (i.e., became steeper) as more sites frequency-converged. **E**, Histograms of the correlation (Spearman’s  $r_{sp}$ ) between frequency-convergence size and phase-gradient slope for the P-A (left) and A-P (right) gradients (an entry per anterior–posterior route per participant per behavioral condition). As expected, the correlations were predominantly negative for the P-A gradients and predominantly positive for the A-P gradients, indicating that the phase gradients became steeper as more sites frequency-converged. Extended Data Figure 4-1 shows the correlation between the absolute slope of phase gradient (averaged across frequency-convergence sizes) and its average PLV across the 19 frequency bins. Extended Data Figure 4-2 shows the occurrences of the P-A and A-P gradients along each of the three anterior–posterior routes for each participant (per behavioral condition). Extended Data Figure 4-3 shows the distribution of the P-A and A-P gradients across the alpha range (5–15 Hz) along each of the three anterior–posterior routes (per behavioral condition). Extended Data Figure 4-4 shows the within-participant consistency of the alpha frequencies at which the P-A and A-P gradients formed during natural viewing (earlier vs later viewing of a silent nature video). Extended Data Figures 4-5–4-9 plot **D** and **E** separately for each of the three anterior–posterior routes and the five behavioral conditions. Extended Data Figure 4-10 plots **D** separately for three alpha subranges (5–8, 8–12, and 12–15 Hz). Extended Data Figure 4-11 is equivalent to **D**, but the phase gradients were computed without surface-Laplacian transforming the EEG data.

We made a histogram of the 19  $r$  values (computed for the 19 frequency bins) for each participant. We then averaged the histograms across participants separately for the three anterior–posterior routes and the five behavioral conditions. The distributions were consistently bimodal (Fig. 4A–C), indicating that oscillation–frequency convergences were accompanied by two distinct types of phase gradients, the P–A gradients (with negative  $r$  values) and the A–P gradients (with positive  $r$  values).

Notably, in the minimal-visual-stimulation conditions (especially in the eyes-closed conditions), the P–A and A–P gradients were spatially segregated. Through the midline, oscillation–frequency convergences were predominantly accompanied by the P–A gradients, indicated by the dominant peak at a negative  $r$  value (Fig. 4A, top three rows). In contrast, through the left- and right-hemisphere, frequency convergences were predominantly accompanied by the A–P gradients, indicated by the dominant peak at a positive  $r$  value (Fig. 4B,C, top three rows). This spatial segregation disappeared during natural viewing. Frequency convergences were accompanied by about equal numbers of P–A and A–P gradients through the midline and each hemisphere, indicated by the symmetrically bimodal distributions of the  $r$  values (Fig. 4A–C, bottom two rows).

For nearly all participants for all anterior–posterior routes and behavioral conditions, oscillation–frequency convergences were accompanied by both the P–A and A–P gradients forming at different frequencies (Extended Data Fig. 4-2). The frequencies at which the two gradient types formed were not consistent across participants except that in the eyes-closed conditions either gradient type dominated (per anterior–posterior route) across a broad range of frequencies for most participants (Extended Data Fig. 4-3). Nevertheless, there was some within-participant consistency in the frequencies at which the two gradient types formed as the pattern of the negative and positive  $r$  values across frequency bins was significantly correlated between the earlier and later viewing of a silent nature video (Extended Data Fig. 4-4).

We next examined how the P–A and A–P gradients changed as a function of the size of frequency convergence. To consider robust cases of the P–A and A–P gradients (which occurred in specific frequency bins; Extended Data Figs. 4-2, 4-3), we selected the gradients with  $r$  values less than  $-0.6$  (occupying mostly below the lower bimodal peak; Fig. 4A–C, highlighted with red-shaded regions) as representative P–A gradients and those with  $r$  values greater than  $0.6$  (occupying mostly above the upper bimodal peak; Fig. 4A–C, highlighted with blue-shaded regions) as representative A–P gradients. We then separately averaged these samples of the P–A and A–P gradients (taken from frequency bins in which they were robust) across the three anterior–posterior routes, participants, and behavioral conditions. As noted above, it is clear that both the P–A and A–P gradients developed, that is, changed from barely sloped to substantially sloped, as more sites frequency-converged (Fig. 4D). To confirm this observation, we computed the correlation (Spearman's  $r$ ,  $r_{sp}$ ) between frequency-convergence size and phase-gradient slope (the slope of the linear fit going through the origin) separately for the P–A and A–P gradients per anterior–posterior route per participant per behavioral condition. For the P–A gradients, the  $r_{sp}$  values were predominantly negative (Fig. 4E, left) indicating that the negative slopes increased with the increasing frequency-convergence size. For the A–P gradients, the  $r_{sp}$  values were predominantly positive (Fig. 4E, right) indicating that the positive slopes increased with the increasing frequency-convergence size. This confirms that both the P–A and A–P gradients became steeper, that is, both phase gradients developed, as more sites frequency-converged. We further note that the phase gradients were approximately linear when all anterior–posterior sites frequency-converged (Fig. 4D, the darkest line), implying traveling waves propagating in the anterior and posterior directions (see Discussion below). Similar patterns of results were obtained separately in each behavioral condition (Extended Data Figs. 4-5–4-9).

### Are the observed oscillation–frequency convergences an artifact of source mixing (primarily volume conduction) effects?

In scalp-recorded EEG, source mixing (primarily volume conduction) effects are extensive (extending  $>5$  cm; Schaworonkoff and Nikulin, 2022). We used the surface-Laplacian transform to reduce source mixing effects to 1–3 cm (Nunez et al., 1994; Tenke and Kayser, 2012; Cohen, 2014). For the current dataset, we verified that volume conduction effects attenuated within  $\sim 1.2$  times the average interelectrode distance (Menceloglu et al., 2024; Fig. 4). Thus, the observed frequency convergences across four or more sites are unlikely to have been generated by volume conduction effects from a single oscillatory source. Importantly, a theoretical consideration and the characteristics of the phase gradients reasonably rule out the possibility that the observed oscillation–frequency convergences could have been spuriously generated by source mixing effects.

Given that source mixing effects are virtually instantaneous, any volume conducted oscillatory activity from a source detected elsewhere has a phase lag of zero. The phase gradients we observed therefore could not have been generated by source mixing effects. If anything, given the likely presence of at least some source mixing effects (especially between adjacent sites), the actual anterior–posterior phase gradients would have been steeper than what we observed. The reason is that any source mixing effects would reduce observed phase differences. Suppose oscillation at site 2 was ahead of oscillation at site 1 by  $\Delta\theta$ , that is, site 2 =  $A_2 \sin(2\pi ft + \Delta\theta)$  while site 1 =  $A_1 \sin(2\pi ft)$ , where  $A_2$  and  $A_1$  are oscillation amplitudes at site 2 and site 1,  $f$  is the oscillation frequency, and  $t$  is time. Adding the volume conducted oscillation from site 1,  $A_1 v_C \sin(2\pi ft)$ , to oscillation at site 2,  $A_2 \sin(2\pi ft + \Delta\theta)$ , yields  $A' \sin(2\pi ft + \Delta\theta)$ , where:

$$\Delta\theta' = \text{atan}[A_2 \sin(\Delta\theta)/(A_1 v_C + A_2 \cos(\Delta\theta))]. \quad (1)$$

Given that  $\Delta\theta' < \Delta\theta$  (as  $A1_{VC}$  is in the denominator), source mixing effects would always reduce observed phase differences relative to the actual phase differences. Indeed, the slopes of the P-A and A-P gradients decrease by a factor of  $\sim 10$  if we do not reduce source mixing effects by applying the surface-Laplacian transform (compare Fig. 4D with Extended Data Fig. 4-11).

Furthermore, if oscillation-frequency convergences were driven by source mixing effects from a prominent source, frequency convergences across more sites would be driven by more extensive source mixing effects from stronger oscillation at the source. Stronger source mixing effects (e.g., larger  $A1_{VC}$  in the above example) would have made the phase gradients less steep (see Eq. 1, having  $A1_{VC}$  in the denominator). To the contrary, we observed that the phase gradients became steeper as more sites frequency-converged (Fig. 4D,E).

## Discussion

Neural communication can be controlled by adjusting phase relations when activities in multiple regions oscillate at a matched frequency. We investigated how oscillation frequencies dynamically converged across regions. We focused on oscillation-frequency convergences along the anterior–posterior axis partly because anatomical, neurophysiological, and functional features exhibit systematic gradients along the anterior–posterior axis (Burt et al., 2018; Huntenburg et al., 2018; Mahjoory et al., 2020) and partly because anterior–posterior neural interactions have been implicated in a variety of perceptual, attentional, and memory processes (de Pasquale et al., 2012; Gonzalez-Castillo and Bandettini, 2018; Lobier et al., 2018; Marzetti et al., 2019; Reinhart and Nguyen, 2019; Mashour et al., 2020). We focused on an extended alpha range (5–15 Hz) because theta, alpha, and low-beta band oscillations are thought to be involved in organizing gamma-oscillation activity (Bahramisharif et al., 2013; Esghaei et al., 2022), controlling information flows (Jensen et al., 2014; Muller et al., 2018; Zhang et al., 2018), and mediating perceptual, attentional, and memory processes (Palva and Palva, 2007; Busch and VanRullen, 2010; Mathewson et al., 2010; Klimesch, 2012; Bonnefond and Jensen, 2015; Fries, 2015; Harris et al., 2018; Lobier et al., 2018; Reinhart and Nguyen, 2019). As we were interested in spontaneous oscillation-frequency convergences, participants rested with their eyes open or closed. To reveal any topographic characteristics, we examined oscillation-frequency convergences along three anterior–posterior routes, through the midline and each hemisphere.

What mechanisms drive anterior–posterior oscillation-frequency convergences? We showed that the probability of an additional site joining a frequency convergence monotonically increased as the size of frequency convergence increased, suggesting that entrainment of additional regions facilitates its spreading. We further showed that oscillatory power at each site increased as it participated in a more extensive frequency convergence. These results are consistent with the idea that anterior–posterior oscillation-frequency convergences are driven by inter-regional entrainment that reciprocally enhances within-region synchronization, which in turn facilitates further inter-regional spreading of entrainment. Future research may investigate what mechanisms trigger the process of inter-regional entrainment that leads to extensive anterior–posterior frequency convergence.

Notably, oscillation-frequency convergences were accompanied by two distinct phase gradients: the P-A gradients (with more anterior sites more phase lagged) and the A-P gradients (with more posterior sites more phase lagged). These gradients were minimal when only two sites frequency-converged but developed into robust approximately linear gradients when all anterior–posterior sites frequency-converged. This coemergence of frequency convergence and phase gradient suggests that they are generated by common mechanisms, which may be investigated in future research.

Regarding the potential functions of the frequency-convergence contingent phase gradients, the P-A gradients may facilitate information flows from posterior to anterior regions in the sense that oscillations ahead in phase could be driving those behind in phase. Similarly, the A-P gradients may facilitate information flows from anterior to posterior regions. Given that the phase gradients (on average) were approximately linear when all anterior–posterior sites frequency-converged and given that the scalp sites along the three anterior–posterior routes (the midline, left-hemisphere, and right-hemisphere routes) were approximately evenly spaced, the frequency-convergence contingent phase gradients imply traveling waves. The phase gradients accompanying full anterior–posterior frequency convergences traversed approximately  $\pm\pi$  radians from the posterior-most to anterior-most site (Fig. 4D) in different subranges of the alpha band (Extended Data Fig. 4-10, darkest curves). Given that the anterior–posterior routes spanned  $\sim 0.24$  m along the scalp, the speed of the putative traveling waves ranged from  $\sim 2.4$  m/s at 5 Hz to  $\sim 7.2$  m/s at 15 Hz. This falls within the range (1–10 m/s) previously reported in macroscopic electrophysiological (i.e., EEG/MEG) recordings (Patten et al., 2012; Muller et al., 2018). The fact that frequency convergences were accompanied by both the P-A and A-P gradients at different alpha frequencies along each of the three anterior–posterior routes suggests that alpha band traveling waves propagate in the posterior-to-anterior (feedforward) and anterior-to-posterior (feedback) directions at different alpha frequencies through the midline as well as through the left and right hemispheres.

During natural viewing, the frequency-convergence contingent P-A and A-P gradients formed at different alpha frequencies (specific to individuals) evenly along each of the three anterior–posterior routes. Interestingly, under minimal visual stimulation, especially when the eyes were closed, the P-A gradients predominantly formed along the midline route, whereas the A-P gradients predominantly formed along the left- and right-hemisphere routes. This suggests that, whereas during natural viewing frequency convergences facilitate both feedforward and feedback flows of alpha band traveling waves through each of the three anterior–posterior routes, when the eyes are closed, feedforward flows are predominantly channeled through the midline

while feedback flows are predominantly channeled through each hemisphere. Future research may investigate how eye closure organizes information flow in this way and how it influences hierarchical information processing.

Prior studies examining traveling waves in the alpha and other frequency bands in EEG reported that they tended to propagate from posterior to anterior regions when the eyes were open and from anterior to posterior regions when the eyes were closed (Alexander et al., 2013; Alamia and VanRullen, 2019). We did not find this asymmetry, but there is an important methodological difference between those studies and the current study. The prior studies identified traveling waves by detecting periods of spatiotemporally linear phase relations. They would have detected traveling waves when the oscillation frequencies were converged along their traveling paths (as in the current study) such as (1) when a single oscillatory population excited more distant neural populations with greater delays and/or (2) when an oscillatory excitation spread by sequentially (with a constant delay) activating a chain of neural populations. However, they would have also detected traveling waves when oscillation frequencies were not converged along their traveling path such as (3) when a chain of oscillatory neural populations influenced one another to generate a spatial gradient of oscillation frequencies wherein a wave travels from higher-frequency populations to lower-frequency populations (Ermentrout and Kleinfeld, 2001). It is possible that a large proportion of traveling waves detected in EEG recordings are generated by Mechanism 3, which would not be accompanied by frequency convergence. We suspect that those traveling waves dominated the results of the prior studies. In contrast, we selectively detected traveling waves accompanying oscillation-frequency convergences [e.g., those generated by Mechanism(s) 1 and/or 2 above]. Future research may investigate the functional roles of frequency-convergence contingent traveling waves in contrast to those generated by other mechanisms.

In summary, alpha oscillation frequencies spontaneously converge along the anterior–posterior axis while people rest, likely driven by inter-regional entrainment. Frequency convergences were accompanied by opposing phase gradients reflective of feedforward and feedback traveling waves which became spatially segregated when the eyes were closed. Future research may investigate the mechanisms that (1) trigger the inter-regional entrainment leading to large frequency convergences, (2) generate the associated phase gradients in specific directions, and (3) spatially segregate the opposing phase gradients upon eye closure, as well as the functional roles of frequency-convergence contingent traveling waves.

## References

- Alamia A, VanRullen R (2019) Alpha oscillations and traveling waves: signatures of predictive coding? *PLoS Biol* 17:e3000487.
- Alexander DM, et al. (2013) Traveling waves and trial averaging: the nature of single-trial and averaged brain responses in large-scale cortical signals. *Neuroimage* 73:95–112.
- Amor F, Rudrauf D, Navarro V, N'diaye K, Garnero L, Martinerie J, Le Van Quyen M (2005) Imaging brain synchrony at high spatio-temporal resolution: application to MEG signals during absence seizures. *Signal Process* 85:2101–2111.
- Bahramisharif A, van Gerven MAJ, Aarnoutse E, Mercier MR, Schwartz TH, Foxe JJ, Ramsey NF, Jensen O (2013) Propagating neocortical gamma bursts are coordinated by traveling alpha waves. *J Neurosci* 33:18849–18854.
- Benwell CSY, London RE, Tagliabue CF, Veniero D, Gross J, Keitel C, Thut G (2019) Frequency and power of human alpha oscillations drift systematically with time-on-task. *Neuroimage* 192:101–114.
- Bonnefond M, Jensen O (2015) Gamma activity coupled to alpha phase as a mechanism for top-down controlled gating. *PLoS One* 10:e0128667.
- Burt JB, Demirtas M, Eckner WJ, Navejar NM, Ji JL, Martin WJ, Bernacchia A, Anticevic A, Murray JD (2018) Hierarchy of transcriptional specialization across human cortex captured by structural neuroimaging topography. *Nat Neurosci* 21:1251–1259.
- Busch NA, VanRullen R (2010) Spontaneous EEG oscillations reveal periodic sampling of visual attention. *Proc Natl Acad Sci U S A* 107:16048–16053.
- Buzsaki G (2006) *Rhythms of the brain*. New York, NY: Oxford University Press.
- Chapeton JI, Haque R, Wittig JH, Inati SK, Zaghloul KA (2019) Large-scale communication in the human brain is rhythmically modulated through alpha coherence. *Curr Biol* 29:2801–2811.
- Chiang AKI, Rennie CJ, Robinson PA, van Albada SJ, Kerr CC (2011) Age trends and sex differences of alpha rhythms including split alpha peaks. *Clin Neurophysiol* 122:1505–1517.
- Cohen MX (2014) *Analyzing neural time series data: theory and practice*. Cambridge, MA: MIT Press.
- Cohen MX (2015) Comparison of different spatial transformations applied to EEG data: a case study of error processing. *Int J Psychophysiol* 97:245–257.
- Cottareau BR, Ales JM, Norcia AM (2015) How to use fMRI functional localizers to improve EEG/MEG source estimation. *J Neurosci Methods* 250:64–73.
- Delorme A, Makeig S (2004) EEGLAB: an open source toolbox for analysis of single-trial EEG dynamics including independent component analysis. *J Neurosci Methods* 134:9–21.
- de Pasquale F, Penna SD, Snyder AZ, Marzetti L, Pizzella V, Romani GL, Corbetta M (2012) A cortical core for dynamic integration of functional networks in the resting human brain. *Neuron* 74:753–764.
- Donoghue T, et al. (2020) Parameterizing neural power spectra into periodic and aperiodic components. *Nat Neurosci* 23:1655–1665.
- Ermentrout GB, Kleinfeld D (2001) Traveling electrical waves in cortex: insights from phase dynamics and speculation on a computational role. *Neuron* 29:33–44.
- Esgளை M, Treue S, Vidyasagar TR (2022) Dynamic coupling of oscillatory neural activity and its roles in visual attention. *Trends Neurosci* 45:323–335.
- Fries P (2005) A mechanism for cognitive dynamics: neural communication through neural coherence. *Trends Cogn Sci* 9:474–480.
- Fries P (2015) Rhythms for cognition: communication through coherence. *Neuron* 88:220–235.
- Gao R, Peterson EJ, Voytek B (2017) Inferring synaptic excitation/inhibition balance from field potentials. *Neuroimage* 158:70–78.
- Gonzalez-Castillo J, Bandettini PA (2018) Task-based dynamic functional connectivity: recent findings and open questions. *Neuroimage* 180:526–533.
- Harris AM, Dux PE, Mattingley JB (2018) Detecting unattended stimuli depends on the phase of prestimulus neural oscillations. *J Neurosci* 38:3092–3101.
- He BJ (2014) Scale-free brain activity: past, present, and future. *Trends Cogn Sci* 18:480–487.
- Hess RF, Snowden RJ (1992) Temporal properties of human visual filters: number, shapes and spatial covariance. *Vision Res* 32:47–60.

- Hjorth B (1980) Source derivation simplifies topographical EEG interpretation. *Am J EEG Technol* 20:121–132.
- Huntenburg JM, Bazin PL, Margulies DS (2018) Large-scale gradients in human cortical organization. *Trends Cogn Sci* 22:21–31.
- Jensen O, Gips B, Bergmann TO, Bonnefond M (2014) Temporal coding organized by coupled alpha and gamma oscillations prioritize visual processing. *Trends Neurosci* 37:357–369.
- Kayser J, Tenke CE (2006) Principal components analysis of Laplacian waveforms as a generic method for identifying ERP generator patterns: i. Evaluation with auditory oddball tasks. *Clin Neurophysiol* 117:348–368.
- Keitel A, Gross J (2016) Individual human brain areas can be identified from their characteristic spectral activation fingerprints. *PLoS Biol* 14:e1002498.
- Klimesch W (2012) Alpha-band oscillations, attention, and controlled access to stored information. *Trends Cogn Sci* 16:606–617.
- Lobier M, Palva JM, Palva S (2018) High-alpha band synchronization across frontal, parietal and visual cortex mediates behavioral and neuronal effects of visuospatial attention. *Neuroimage* 165:222–237.
- Lopez-Calderon J, Luck SJ (2014) ERPLAB: an open-source toolbox for the analysis of event-related potentials. *Front Hum Neurosci* 8:213.
- Lui LL, Bourne JA, Rosa MGP (2007) Spatial and temporal frequency selectivity of neurons in the middle temporal visual area of new world monkeys (*Callithrix jacchus*). *Eur J Neurosci* 25:1780–1792.
- Mahjoory K, Schoffelen J-M, Keitel A, Gross J (2020) The frequency gradient of human resting-state brain oscillations follows cortical hierarchies. *Elife* 9:e53715.
- Mallat S (2009) *A wavelet tour of signal processing: the sparse way*. Burlington, MA: Academic Press.
- Marzetti L, Basti A, Chella F, D'Andrea A, Syrjälä J, Pizzella V (2019) Brain functional connectivity through phase coupling of neuronal oscillations: a perspective from magnetoencephalography. *Front Neurosci* 13:964.
- Mashour GA, Roelfsema P, Changeux J-P, Dhaene S (2020) Conscious processing and the global neuronal workspace hypothesis. *Neuron* 105:776–798.
- Mathewson KE, Gratton G, Fabiani M, Beck DM, Ro T (2010) To see or not to see: prestimulus alpha phase predicts visual awareness. *J Neurosci* 29:2725–2732.
- Menceloglu M, Grabowecy M, Suzuki S (2020a) Spectral-power associations reflect amplitude modulation and within-frequency interactions on the sub-second timescale and cross-frequency interactions on the seconds timescale. *PLoS One* 15:e0228365.
- Menceloglu M, Grabowecy M, Suzuki S (2020b) EEG state-trajectory instability and speed reveal global rules of intrinsic spatiotemporal neural dynamics. *PLoS One* 15:e0235744.
- Menceloglu M, Grabowecy M, Suzuki S (2021a) Spatiotemporal dynamics of maximal and minimal EEG spectral power. *PLoS One* 16:e0253813.
- Menceloglu M, Grabowecy M, Suzuki S (2021b) Probabilistic, entropy-maximizing control of large-scale neural synchronization. *PLoS One* 16:e0249317.
- Menceloglu M, Grabowecy M, Suzuki S (2024) A phase-shifting anterior-posterior network organizes global phase relations. *PLoS One* 19:e0296827.
- Mierau A, Klimesch W, Lefebvre J (2017) State-dependent alpha peak frequency shifts: experimental evidence, potential mechanisms, and functional implications. *Neuroscience* 360:146–154.
- Muller L, Chavane F, Reynolds J, Sejnowski TJ (2018) Cortical traveling waves: mechanisms and computational principles. *Nat Rev Neurosci* 19:255–268.
- Nunez PL, Silberstein RB, Cadusch PJ, Wijesinghe RS, Westdorp AF, Srinivasan R (1994) A theoretical and experimental study of high resolution EEG based on surface Laplacians and cortical imaging. *Electroencephalogr Clin Neurophysiol* 90:40–57.
- Nunez P, Srinivasan R (2006) *Electric fields of the brain: the neurophysics of EEG*. New York, NY: Oxford University Press.
- Palva S, Palva JM (2007) New vistas for  $\alpha$ -frequency band oscillations. *Trends Neurosci* 30:150–158.
- Palva S, Palva JM (2012) Discovering oscillatory interaction networks with M/EEG: challenges and breakthroughs. *Trends Cogn Sci* 16:219–230.
- Palva JM, Palva S, Kaila K (2005) Phase synchrony among neuronal oscillations in the human cortex. *J Neurosci* 25:3962–3972.
- Patten TM, Rennie CJ, Robinson PA, Gong P (2012) Human cortical traveling waves: dynamical properties and correlations with responses. *PLoS One* 7:e38392.
- Perrin F, Pernier J, Bertrand O, Echallier JF (1989) Spherical splines for scalp potential and current density mapping. *Electroencephalogr Clin Neurophysiol* 72:184–187.
- Perrin F, Pernier J, Bertrand O, Echallier JF (1990) Corrigenda EEG 02274. *Electroencephalogr Clin Neurophysiol* 76:565.
- Perrin F, Pernier J, Bertrand O, Giard MH, Echallier JF (1987) Mapping of scalp potentials by surface spline interpolation. *Electroencephalogr Clin Neurophysiol* 66:75–81.
- Reinhart RMG, Nguyen JA (2019) Working memory revived in older adults by synchronizing rhythmic brain circuits. *Nat Neurosci* 22:820–827.
- Rudrauf D, Douiri A, Kovach C, Lachaux J-P, Cosmelli D, Chavez M, Adam C, Renault B, Martinerie J, Le Van Quyen M (2006) Frequency flows and the time-frequency dynamics of multivariate phase synchronization in brain signals. *Neuroimage* 31:209–227.
- Schaworonkoff N, Nikulin VV (2022) Is sensor space analysis good enough? Spatial patterns as a tool for assessing spatial mixing of EEG/MEG rhythms. *Neuroimage* 253:119093.
- Smith MK, Grabowecy M, Suzuki S (2024) Dynamic formation of a posterior-to-anterior peak-alpha-frequency gradient driven by two distinct processes. *eNeuro* 11:ENEURO.0273-24.2024.
- Tenke CE, Kayser J (2012) Generator localization by current source density (CSD): implications of volume conduction and field closure at intracranial and scalp resolutions. *Clin Neurophysiol* 123:2328–2345.
- Tewarie P, Hunt BA, O'Neill GC, Byrne A, Aquino K, Bauer M, Mullinger KJ, Coombes S, Brookes MJ (2019) Relationships between neuronal oscillatory amplitude and dynamic functional connectivity. *Cereb Cortex* 29:2668–2681.
- van Albada SJ, Robinson PA (2013) Relationships between electroencephalographic spectral peaks across frequency bands. *Front Hum Neurosci* 7:56.
- Zhang H, Watrous AJ, Patel A, Jacobs J (2018) Theta and alpha oscillations are traveling waves in the human neocortex. *Neuron* 98:1269–1281.